Analysis of CT Perfusion Blood Flow Maps in Patients with Lung Cancer: Correlation with the Overall Survival

Serena Baiocco*✉, Domenico Barone†, Giampaolo Gavelli†, Alessandro Bevilacqua*
* University of Bologna, Bologna, Italy
†IRCCS - Istituto Scientifico Romagnolo per lo Studio e la Cura dei Tumori (IRST), Meldola (FC), Italy
{s.baiocco, alessandro.bevilacqua}@unibo.it, {d.barone, g.gavelli}@irst.emr.it

***Abstract*—Computed Tomography perfusion (CTp) is a functional imaging technique with a wide application in the oncological field. CTp allows detecting the presence of tumour abnormal hemodynamic patterns, by analysing the tissue temporal variations occurring after the administration of the contrast medium. This work presents a novel approach to extract meaningful features from blood flow (BF) maps of lung cancers, which could act as a prognostic image-based biomarker.**

I. Introduction

Lung cancer is the most common malignant disease and the leading cause of cancer death worldwide [1]. 85% of lung cancers are non-small-cell lung cancers (NSCLCs) [2]. Despite the introduction of more advanced therapeutic strategies, including antiangiogenic treatments, NSCLC remains associated with poor prognosis and overall survival (OS) [3]. Tumour staging is recognised as the most important prognostic factor of survival. However, heterogeneity within the same stage grouping suggests individual factors influence survival outcomes [4]. In this era of personalized therapy, one of the challenges remains the identification of more effective markers of prognosis for a better stratification of NSCLC patients [5], with strong implications in treatment choices and consideration of alternative therapies [6].

Several studies have focused on the analysis of the intra-tumoral heterogeneity and the underlying biological mechanisms in order to identify more accurate prognostic biomarkers [7], [8], [9]. Indeed, NSCLC tissues are extremely heterogeneous both at genetic and histopatological level, reflecting the presence of angiogenesis, hypoxia, high cell density, necrosis and hemorrhage [10], [11]. Angiogenesis is a process involving the chaotic proliferation of new blood vessels from pre-existing ones [12], which may cause local reductions in BF thus leading to hypoxia. This is a universal cancer hallmark determining tumour response to treatment in NSCLC, reducing radiosensitivity as well as sensitivity to some chemotherapeutic agents [13].

The presence of the intra-tumoral heterogeneity limits the use of invasive biopsy based on molecular assays, since small bioptic samples could not adequately catch the whole tumour heterogeneity properties. Instead, imaging technologies have the potentiality to capture the intra-tumoral heterogeneity, which can be assessed by developing algorithms able to exploit voxel-based information and derive quantitative tumour tissue information.

Recently, CTp has been accepted as a clinical technique in the oncologic field, primarily for the early evaluation of tumour response to anti-angiogenic therapies [14]. Indeed, CTp allows capturing tumours vascular patterns through the analysis of the time-concentration curves (TCCs), representing the tissue density temporal variations [15], directly proportional to the quantity of contrast medium within the tissue. One of the most effective perfusion parameters is the BF, which proved to detect the earliest functional changes on tumour vasculature even within the first week of anti-angiogenic therapy [16]. Moreover, BF shows a high correlation with the tissue biomarker micro-vessel density (MVD) [17], [18]. The analysis of BF maps could permit the detection of abnormal vascular patterns within tumour tissue. However, several factors may affect the reliability of BF maps. Among these, respiratory and cardiac motion artefacts, especially in abdomen and thorax studies, partial volume artefacts as well as physics-based artefacts, for instance, occurring in tumour located near structures with a high concentration of contrast agent (e.g., heart and great blood vessels) and bony regions of the chest [19]. Therefore, a reliability analysis is needed to properly characterise the tissue heterogeneity and, finally, to derive quantitative features [20].

In this work, we present a novel method to evaluate the intra-tumoral heterogeneity emerging from BF maps. To this purpose, BF maps were computed according to the Maximum-Slope method. A proper reliability analysis of the BF maps was performed to automatically detect and remove those pixels and regions undergoing high computing errors due to artefacts, which could hamper the evaluation of the tissue micro-circulation. Two local-based statistical indexes were developed, able to gather and exploit information owned by the hemodynamic heterogeneity patterns at local level, and expectedly to isolate the effects of variability due to image artefacts and tumour size. At diagnosis, the correlation between the feature-pair computed on BF maps and the OS of patients affected by NSCLC was explored to assess whether these features could work as a prognostic image-based biomarker for NSCLC. The discrimination ability of the feature-pair was analysed in comparison with the staging, a disease variable commonly associated with OS. The new developed features proved a strong correlation with OS, this suggesting a promising prognostic clinical application of CTp.

ISSN 2305-7254

II. Materials and methods

A. Study population

This study was approved by the Institutional Review Board that waived informed consent for the retrospective data analysis of the patients. Between September 2010 and December 2012, a total of 36 consecutive patients (25 men, 11 women; age range 36-81 years) with primary NSCLC, subdivided in 28 AC, 6 SCC and 2 LCC,were enrolled for data analysis. Tumour stage was determined in all patients according to the TNM classification (seventh edition) of malignant tumours: 2 patients were diagnosed stage IB, 3 patients IIIA, 4 patients IIIB and 27 patients IV tumour stage. Patients inclusion criteria were: (a) over eighteen years old, (b) with histologically verified NSCLC, and (c) no prior history of chemotherapy, surgery or thoracic radiation therapy.

Exclusion criteria were: (a) clinically significant cardiovascular disease, (b) pregnancy or lactation, (c) a known history of deep vein thrombus or pulmonary embolus, (d) patients lost to follow-up for unknown reasons ($n = 8$), (e) patients alive at the time of the study ($n = 4$), (f) not having the longest axial diameter of the lesion larger than 10 mm in at least one slice ($n = 3$), and (g) examination severely affected by physics-based artefact ($n = 2$).

The final population included 19 patients. The variable considered as a reference for the survival prediction was the staging. This variable was dichotomised so as to divide in early stage patients likely receiving curative surgery or curative chemoradiotherapy (stage I - IIIA) and advanced stage patients (stage IIIB - IV) likely receiving non-curative chemotherapy, radiotherapy, or molecular therapies.

Table 1 includes the previous information along with the histological subtype (adenocarcinoma, squamous cell carcinoma, large cell carcinoma, NSCLC not otherwise specified, NOS) and patients overall survival (OS) data, defined as the time interval in months between the date of baseline TC examination and the date of death.

TABLE I. Summary of the histological diagnosis, tumour stage and OS data (months) relative to each patient

Patient ID	Diagnosis	Stage	OS
ID1	LCC	IIIB	6
ID2	AC	IV	4
ID3	SCC	IB	14
ID4	AC	IV	13
ID5	AC	IV	5
ID6	AC	IB	5
ID7	AC	IV	6
ID8	AC	IV	10
ID9	SCC	IV	17
ID10	SCC	IV	52
ID11	AC	IV	6
ID12	AC	IV	6
ID13	AC	IV	4
ID14	AC	IV	8
ID15	AC	IV	12
ID16	SCC	IIIB	11
ID17	AC	IV	12
ID18	AC	IV	0
ID19	AC	IV	7

B. CTp protocol

At the diagnosis stage, the patients underwent axial CTp performed on a 256-slice CT system (Brilliance iCT, Philips Medical System, Best, The Netherlands), feet first in the supine position. Initially, an unenhanced low-dose full-body CT scan was performed to identify the target lesions at baseline conditions. Then, a 50 mL intravenous bolus of contrast agent (Iomeron, Bracco, Milan, Italy) was injected at 5 mL/s for axial cine contrast enhanced CT. Each patient performed a single acquisition of duration 25 seconds under breath-hold condition. This protocol yields 20 scans, each corresponding to different sampling instants, with 55 mm of z-coverage (11 slices $\times$ 5-mm slice thickness, 0.4-sec rotation time, at 80 kV, 250 mA). Image data are reconstructed to 220 cine images (512 $\times$ 512 pixel, 11 slices, 350 mm $\times$ 350-mm, 5-mm slice spacing, 1.25-sec temporal resolution).

C. Perfusion maps generation

The target lesions and the arterial input (aorta) were selected in agreement by two radiologists on a reference slice. For each lesion on the reference slice, the radiologists manually drawn the region of interest (ROI) and translated it on the remaining slices of the reference sequence, so that the borders of the lesion visually match. Moreover, when appropriate, adjacent slice levels (up to two levels before and after the reference one) were visually explored by the radiologists who chose, for each scan, the levels which visually offer the best match with the reference slice [21], so as to achieve the "best" sequence as shown in Fig. 1. According to this procedure, a 3D rigid alignment of the lesion in the reference slice is achieved.

BF values were computed by considering the first-pass phase only [22] and representing each voxel with a single-compartment model, including both the intravascular and the interstitial spaces. This allowed performing short-time examinations with the effect of reducing motion artefacts, since patients had the possibility to remain in apnoea. As shown in Fig. 2, the model adopted is characterised by a single inlet, the arterial input, with an arterial blood plasma temporal concentration $C_A(t)$, and a single outlet, the venous outlet, with a venous blood plasma temporal concentration $C_V(t)$. $C_T(t)$ represents the TCC of the tissue. The relation between $C_A(t)$, $C_V(t)$ and $C_T(t)$ can be expressed through the Fick's principle representing the conservation of mass:

$$\frac{dC_T(t)}{dt} = \frac{BF}{V_T}[C_A(t) - C_V(t)] \tag{1}$$

One immediate approximation consists in the assumption of no venous outflow during the measurement period $C_V(t) \simeq 0$ (i.e., no contrast agent has reached the venous side of the circulation yet). This is valid only if the time periods are less than the minimum transit time, that is when the injected contrast agent will all remain inside the tissue. Under this assumption, Eq. (1) can be simplified as follows:

$$\frac{dC_T(t)}{dt} = \frac{BF}{V_T}[C_A(t) - C_V(t)] \simeq \frac{BF}{V_T}C_A(t) \tag{2}$$

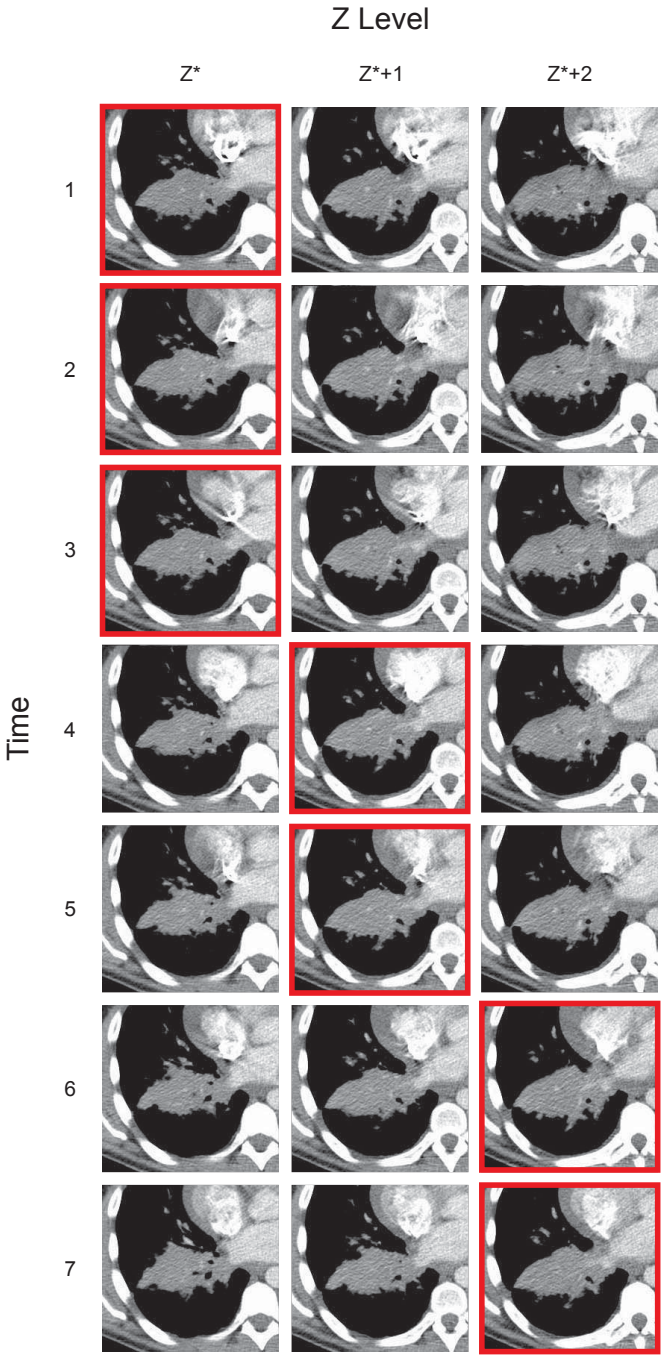

Fig. 1. Example of selection of the best sequence for a lung tumour perfusion study, performed to achieve the best matching with the Z levels contiguous with the reference slice level, represented by Z^*

This implies that the slope of the tissue curve, $dC_T(t)/dt$, reaches a maximum (steepest slope) when the TCC of the arterial input, $C_A(t)$, reached is peak density [23]. Thus, the BF, expressed in mL/min/100 g, is given by

$$\frac{BF}{V_T} \simeq \frac{[\frac{dC_T(t)}{dt}]_{max}}{[C_A(t)]_{max}} \tag{3}$$

This is the well-known Mullani-Gould model or single-compartment formulation. The simplification adopted in Eq. (2) results in an overestimation of the denominator of Eq. (3), and consequently in an underestimation of the BF whether the bolus is large, or for organs with a fast vascular transit. Accordingly, for organs characterised by a complex microcirculation, such as kidney and spleen, this assumption might not hold [24], but for most clinical applications this formulation results adequate with appropriate accuracy and precision levels [25]. BF values can be visualised through the use of functional colorimetric maps.

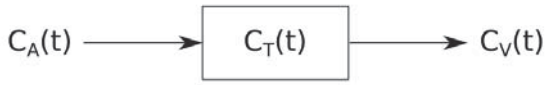

Fig. 2. Single-compartment model representing the tissue perfusion

In order to obtain the TCC signal for each voxel, several approaches are proposed in the literature [26]. In this work, we adopted a sigmoid-shape model given by the *Hill Equation* in Eq. (4), able to fit the main trend of the concentration samples in a robust manner [27]:

$$\overline{Y}_{TCC}(t) = E_0 + (E_{max} - E_0)\frac{t^\alpha}{(EC_{50} + t)^\alpha} \tag{4}$$

where E_0 is the baseline concentration of the tissue, that is before the arrival of the tracer, E_{max} is the saturation value of the concentration reached after its arrival, EC_{50} is the time instant at the half-maximum value of the concentration, and α is the parameter which mainly affects the slope of the sigmoid curve. The curve fitting is achieved using an in-house fitting algorithm based on the nonlinear, least squares, Levenberg-Marquardt minimization algorithm (lsqcurvefit, Matlab©; MathWorks, Natick, MA, USA).

D. Perfusion maps denoising

The analysis of tumours BF maps includes a denoising process, consisting in detecting and excluding unreliable BF values, a necessary step to be performed before the local analysis and features extraction. Basically, BF values strictly lower than 1 mL/min/100 g were automatically removed, being considered unlikely as physiological values and rather attributable to numerical errors, as the algorithm of perfusion computation forces the values to be positive.

The quality of the fitting has been assessed by considering the residuals (ϵ) of each TCC signal, measured as the difference between the observed samples Y_{TCC} and the relative values computed through the fitting $\overline{Y}_{TCC}$ for each time instant t. ϵ is defined as in Eq. (5):

$$\epsilon(t) = \left|Y_{TCC}(t) - \overline{Y}_{TCC}(t)\right| \tag{5}$$

Being ϵ directly proportional to the distance between the detected and the computed sample, it will highlight the differences among these samples. The reliability of the single TCC has been assessed by computing the temporal mean value μ_ϵ of the residual ϵ relative to the considered pixel. The distribution

of this error has been used to detect those BF values underwent high fitting errors in order to exclude them from the analysis, since they derive from TCCs not correctly fitted.

High errors usually occur in the presence of noise, artefacts (both physics and due to motion) and anatomical structures, such as bronchi and blood vessels. Through the use of this index, these structures usually manually removed, can be automatically excluded from the analysis by adopting a cut-off value. Several kind of thresholds can be adopted to exclude unreliable values from the analysis of the BF maps. In this work the "triangle" method reported in [28] has been adopted. At the end of these automatic procedures, the removed BF values appear highlighted in the colour maps with the pink colour, as shown in Fig. 3. As one can see, the denoising method removes unreliable regions also including the edge ones, which are affected by partial volume effect, still preserving a wide range of BF values [29].

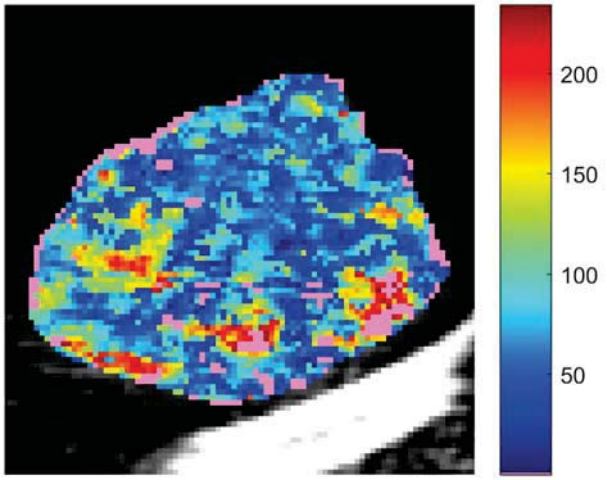

Fig. 3. BF colorimetric map of an adenocarcinoma examination (patient ID8). The pink colour points out unreliable BF values

E. Computation of novel local-based features

After denoising, the functional heterogeneity arising from lesions' BF maps was assessed using an in-house software developed in Matlab© (MathWorks, Natick, MA, USA).

In order to analyse the functional heterogeneity we chose entropy (*E*), the first-order statistics feature commonly used to measure image irregularity or randomness [30], which has recently shown a huge prognostic potential in patients with colorectal cancer [31], gliomas [32] and breast cancer [33]. *E* is defined as in Eq. (6):

$$E = -\sum_{i=1}^{L} p_i \ \log_2 p_i \tag{6}$$

where $p_i = \frac{h_i}{N}$ is the occurrence probability for the intensity level i with a frequency h_i, in an image with N pixels and L intensity levels.

The analysis was computed locally on denoised BF maps, within the same ROI drawn for the perfusion map computation, by using a window *W* centred on the pixel that will be replaced with the resulting value. The choice of *W*, representing the anatomical scale considered to perform the local analysis, was first driven by the radiologists of our team, stating that in the clinical practice patches smaller than 5×5 mm are rarely considered and patches of about 1×1 cm are more representative for NSCLC functional heterogeneity. On the other hand, it is well known that CT texture features finer than 4 mm would represent noise and should not be considered [5]. For this reason, entropy was computed locally for each pixel of the BF map, considering a square region with side of 15 pixels, corresponding to 1.03 cm, centred on the pixel itself. This procedure was iteratively repeated for each pixel within the ROI by using the sliding window *W*. At the end, a local entropy (*locE*) map was achieved and the mean value of *locE* maps, μE, was considered as a feature of the functional heterogeneity. As an example, Fig. 4 shows the *locE* map relative to the BF map in Fig. 3. As one can see, the *locE* map highlights the presence of a greater heterogeneity in the lower region of the tumour, caused by the presence of the small areas with different tissue density characterising the BF map.

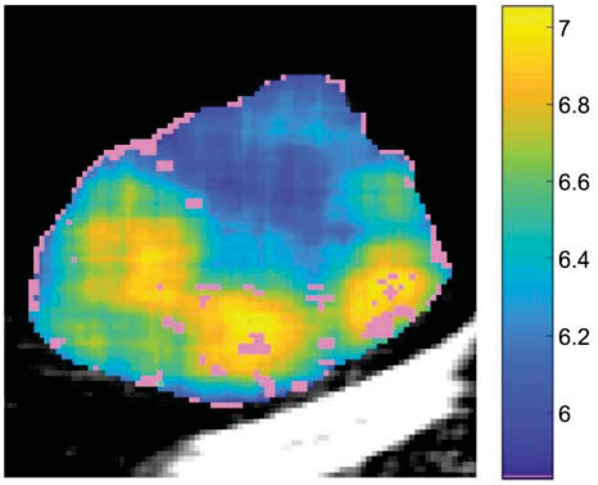

Fig. 4. *locE* map highlighting a high heterogeneity of the BF values in the lower region of the tumour (patient ID8)

The great advantage of performing a local analysis and, then, considering the mean values of the local feature values, is that it heavily reduces the effects of tumour size on statistical measurements.

We also explore the clinical potentiality of the other first-order statistics features (mean, standard deviation, median, skewness, kurtosis, and uniformity) focusing on uniformity (*U*), a feature related to the image homogeneity, showing high values in the presence of small BF transitions in the map. *U* is defined as in Eq. (7):

$$U = \sum_{i=1}^{L} p_i^2 \tag{7}$$

Also in this case, we considered the mean value of the local uniformity (*locU*) maps, μU, as a feature of the tumour functional heterogeneity. As an example, Fig. 5 shows the *locU*

map relative to the BF map reported in Fig. 3. The high values of the *locU* map in the upper region of the tumour point out the presence of a homogeneous hypodense area. It is worth noting that *locE* and *locU* values are inversely related but not linearly dependent.

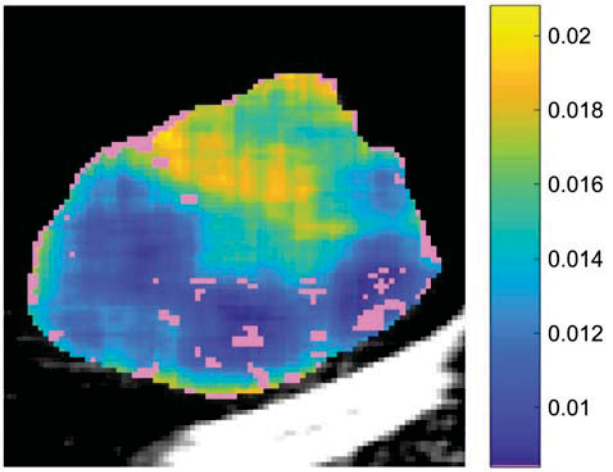

Fig. 5. *locU* map highlighting an increased uniformity of BF values in the upper region of the tumour (patient ID8)

F. Statistical Analysis

The principal purpose of this work was to determine whether local features directly extracted from denoised BF maps could work as a surrogate prognostic biomarker. To avoid overfitting, the features selected were analysed both separately as well as jointly in pairs. In order to assess their prognostic potential, the correlation between the feature-pair and the overall survival (OS) was investigated by using the *k*-means clustering algorithm. Mean survival for the entire cohort of patients ($\mu_{OS} = 10.5$) was used as threshold to separate patients with highest ($OS \geq \mu_{OS}$) and lowest ($OS < \mu_{OS}$) survival expectation. *k*-means ($k = 2$) was set up so as to automatically group patients in two different classes (or clusters), characterised by similar features behaviour. As similarity measure to resolve the membership of the feature-pairs, the Squared Euclidean distance was considered. In order to determine to what extent the feature means differ between clusters identified by the algorithm, a multivariate analysis of variance (MANOVA) was performed (p-value < 0.001). Sensitivity (SE), specificity (SP), positive predictive value (PPV), negative predictive value (NPV) and accuracy (ACC) were calculated to quantify the discrimination ability of both features selected and staging, which is the variable used as reference for survival prediction. In particular, we defined as condition true a low survival expectation and as condition false a high survival expectation. The positive prediction is represented by the advanced stage condition while the negative prediction by the early stage one. Therefore, patients with advanced stage and low survival expectation belong to the true positive (TP), patients with early stage characterised by a high survival expectation are the true negative (TN), while the patients with advanced stage and a high survival expectation are the false positive (FP), and the patients with an early stage and a low survival expectation are the false negative (FN).

Statistical analysis was performed using Matlab© (MathWorks, Natick, MA, USA).

III. Results

μE and μU are the features characterised by the highest discriminatory power in distinguishing patients with different survival expectations (SE=100%, SP=71%, PPV=86%, NPV=100%, ACC=90%). Results in terms of μE and μU for each patient are summarized and reported in arbitrary units (a.u.) in Table II.

TABLE II. Summary of μE and μU relative to each examination (ID), reported in arbitrary units (a.u.)

Patient ID	μE [a.u.]	μU $(\cdot 10^{-2})[a.u.]$
ID1	6.00	1.92
ID2	6.59	1.22
ID3	4.62	5.20
ID4	6.70	1.12
ID5	6.81	1.01
ID6	6.56	1.21
ID7	6.13	1.69
ID8	6.45	1.36
ID9	5.78	2.24
ID10	5.38	3.09
ID11	6.32	1.44
ID12	6.61	1.19
ID13	6.14	1.70
ID14	6.71	1.11
ID15	6.23	1.57
ID16	5.75	2.23
ID17	5.82	2.14
ID18	6.34	1.46
ID19	6.61	1.13

μE and μU are able to group patients with the lowest ($OS < \mu_{OS}$) and highest ($OS \geq \mu_{OS}$) survival expectation. Cluster 1 (highlighted in red in Fig. 6), characterized by higher μE and lower μU values, encloses all the patients with the worst prognosis ($OS < \mu_{OS}$), with the exception of ID4 and ID15 pointed out in Fig. 6.

On the contrary, the samples belonging to the Cluster 2 (highlighted in blue in Fig. 6) referred to all patients characterised by the best prognosis in this study ($OS \geq \mu_{OS}$). The outcome of MANOVA proves that μE and μU of the two clusters differ significantly, with a p-value $= 1.2 \cdot 10^{-4}$.

Staging (SE=92%, SP=14%, PPV=65%, NPV=50%, ACC=63%) performed worse as survival predictor.

IV. Conclusion

In the last decade, quantifying the perceived features of the intra-tumoral heterogeneity has gained a great attention, leading to a renewed interest for statistical features and texture analysis as essential tools in the era of personalised medicine. First-order statistics features widely used in literature [34], [35] do not take into account the spatial information of the images

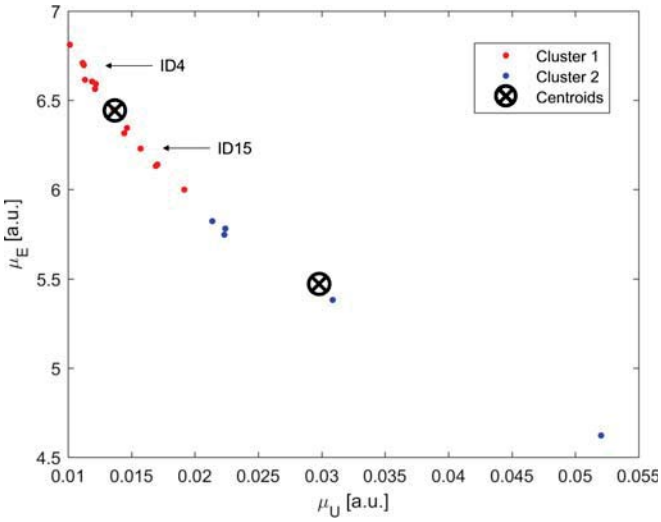

Fig. 6. Scatter plot of μE and μU values related to all the examinations are reported in arbitrary units (a.u.). 14 examinations belong to Cluster 1 (in red), 5 to Cluster 2 (in blue)

but just the distribution of values. Therefore, when computing first-order features tissue heterogeneity information within an image is almost disregarded. The local features we devised preserve the tissue heterogeneity information within the considered ROI. Results showed that these features have a valuable prognostic potential, proving a high correlation with OS when computed on BF maps, where unreliable BF values have been previously automatically removed. In particular, a greater heterogeneity of BF values seems to be associated with a higher tumour aggressiveness, which heavily affects the OS parameter. It is worth noting that this approach can be easily performed retrospectively on CT data routinely acquired in clinical practice, without the need for additional examinations and maximising the information that can be derived from these studies.

REFERENCES

[1] Zhao Chen, Christine M Fillmore, Peter S Hammerman, Carla F Kim, and Kwok-Kin Wong. Non-small-cell lung cancers: a heterogeneous set of diseases. *Nat. Rev. Cancer*, 14(8):535–546, 2014.

[2] Yanyan Xu, Hongliang Sun, Zhenrong Zhang, Aiping Song, Wu Wang, and Xiaomei Lu. Assessment of relationship between CT features and serum tumor marker index in early-stage lung adenocarcinoma. *Acad. Radiol.*, 23(11):1342–1348, 2016.

[3] Martin Reck, David F Heigener, Tony Mok, Jean-Charles Soria, and Klaus F Rabe. Management of non-small-cell lung cancer: recent developments. *Lancet*, 382(9893):709–719, 2013.

[4] Marliese Alexander, Rory Wolfe, David Ball, Matthew Conron, Robert G Stirling, Benjamin Solomon, Michael MacManus, Ann Officer, Sameer Karnam, Kate Burbury, et al. Lung cancer prognostic index: a risk score to predict overall survival after the diagnosis of non-small-cell lung cancer. *British journal of cancer*, 117(5):744, 2017.

[5] Balaji Ganeshan, Elleny Panayiotou, Kate Burnand, Sabina Dizdarevic, and Ken Miles. Tumour heterogeneity in non-small cell lung carcinoma assessed by CT texture analysis: a potential marker of survival. *Eur. Radiol.*, 22(4):796–802, 2012.

[6] Stephen G Spiro, Nichole T Tanner, Gerard A Silvestri, Sam M Janes, Eric Lim, Johan F Vansteenkiste, and Robert Pirker. Lung cancer: progress in diagnosis, staging and therapy. *Respirology*, 15(1):44–50, 2010.

[7] Philippe Lambin, Emmanuel Rios-Velazquez, Ralph Leijenaar, Sara Carvalho, Ruud GPM van Stiphout, Patrick Granton, Catharina ML Zegers, Robert Gillies, Ronald Boellard, André Dekker, and Aerts Hugo J. Radiomics: extracting more information from medical images using advanced feature analysis. *Eur. J. Cancer*, 48(4):441–446, 2012.

[8] Connie Yip, David Landau, Robert Kozarski, Balaji Ganeshan, Robert Thomas, Andriana Michaelidou, and Vicky Goh. Primary esophageal cancer: heterogeneity as potential prognostic biomarker in patients treated with definitive chemotherapy and radiation therapy. *Radiology*, 270(1):141–148, 2014.

[9] Francesca Ng, Balaji Ganeshan, Robert Kozarski, Kenneth A Miles, and Vicky Goh. Assessment of primary colorectal cancer heterogeneity by using whole-tumor texture analysis: contrast-enhanced CT texture as a biomarker of 5-year survival. *Radiology*, 266(1):177–184, 2013.

[10] Fergus Davnall, Connie SP Yip, Gunnar Ljungqvist, Mariyah Selmi, Francesca Ng, Bal Sanghera, Balaji Ganeshan, Kenneth A Miles, Gary J Cook, and Vicky Goh. Assessment of tumor heterogeneity: an emerging imaging tool for clinical practice? *Insights into imaging*, 3(6):573–589, 2012.

[11] Alessandro Bevilacqua and Serena Baiocco. Automatic classification of lung tumour heterogeneity according to a visual-based score system in dynamic contrast enhanced CT sequences. *Int. J. Mod. Phys. C*, pages 1650106–1–1650106–14, 2016.

[12] TY Lee, TG Purdie, and E Stewart. CT imaging of angiogenesis. *The Quarterly Journal of Nuclear Medicine and Molecular Imaging*, 47(3):171, 2003.

[13] Balaji Ganeshan and Kenneth A Miles. Quantifying tumour heterogeneity with CT. *Cancer imaging*, 13(1):140, 2013.

[14] Davide Prezzi, Aisha Khan, and Vicky Goh. Perfusion CT imaging of treatment response in oncology. *European journal of radiology*, 84(12):2380–2385, 2015.

[15] G Petralia, L Bonello, S Viotti, L Preda, G d'Andrea, and M Bellomi. CT perfusion in oncology: how to do it. *Cancer Imaging*, 10(1):8–19, 2010.

[16] Nunzia Tacelli, Teresa Santangelo, Arnaud Scherpereel, Alain Duhamel, Valérie Deken, Ernst Klotz, Alexis Cortot, Jean-Jacques Lafitte, Frédéric Wallyn, Jacques Remy, et al. Perfusion CT allows prediction of therapy response in non-small cell lung cancer treated with conventional and anti-angiogenic chemotherapy. *Eur. Radiol.*, 23(8):2127–2136, 2013.

[17] Gaspard d'Assignies, Anne Couvelard, Stéphane Bahrami, Marie-Pierre Vullierme, Pascal Hammel, Olivia Hentic, Alain Sauvanet, Pierre Bedossa, Philippe Ruszniewski, and Valérie Vilgrain. Pancreatic endocrine tumors: tumor blood flow assessed with perfusion CT reflects angiogenesis and correlates with prognostic factors. *Radiology*, 250(2):407–416, 2009.

[18] Avinash Kambadakone, Sam S Yoon, Tae-Min Kim, Daniel L Karl, Dan G Duda, Thomas F DeLaney, and Dushyant V Sahani. CT perfusion as an imaging biomarker in monitoring response to neoadjuvant bevacizumab and radiation in soft-tissue sarcomas: comparison with tumor morphology, circulating and tumor biomarkers, and gene expression. *Am. J. Roentgenol.*, 204(1):W11–8, 2015.

[19] Julia F Barrett and Nicholas Keat. Artifacts in CT: recognition and avoidance. *Radiographics*, 24(6):1679–1691, 2004.

[20] Alessandro Bevilacqua, Domenico Barone, Serena Baiocco, and Giampaolo Gavelli. A novel approach for semi-quantitative assessment of reliability of blood flow values in DCE-CT perfusion. *Biomed. Signal Process. Control*, 31:257–264, 2017.

[21] Alessandro Bevilacqua, Domenico Barone, Silvia Malavasi, and Giampaolo Gavelli. Quantitative assessment of effects of motion compensation for liver and lung tumors in CT perfusion. *Acad. Radiol.*, 21(11):1416–1426, 2014.

[22] Yoshiharu Ohno, Yasuko Fujisawa, Hisanobu Koyama, Yuji Kishida, Shinichiro Seki, Naoki Sugihara, and Takeshi Yoshikawa. Dynamic contrast-enhanced perfusion area-detector CT assessed with various mathematical models: Its capability for therapeutic outcome prediction for non-small cell lung cancer patients with chemoradiotherapy as compared with that of FDG-PET/CT. *Eur. J. Radiol.*, 86:83–91, 2017.

[23] KA Miles and MR Griffiths. Perfusion CT: a worthwhile enhancement? *Br. J. Radiol.*, 76(904):220–231, 2003.

[24] KA Miles. Perfusion CT for the assessment of tumour vascularity: which protocol? *Br. J. Radiol.*, 76(1):S36–42, 2003.

[25] Gunnar Brix, Stefan Zwick, Jürgen Griebel, Christian Fink, and Fabian Kiessling. Estimation of tissue perfusion by dynamic contrast-enhanced imaging: simulation-based evaluation of the steepest slope method. *Eur. Radiol.*, 20(9):2166–2175, 2010.

[26] Mario Sansone, Roberta Fusco, and Antonella Petrillo. A geometrical perspective on the 3TP method in DCE-MRI. *Biomed. Signal Process. Control*, 16:32–39, 2015.

[27] Sylvain Goutelle, Michel Maurin, Florent Rougier, Xavier Barbaut, Laurent Bourguignon, Michel Ducher, and Pascal Maire. The Hill equation: a review of its capabilities in pharmacological modelling. *Fundam. Clin. Pharmacol.*, 22(6):633–648, 2008.

[28] Alessandro Bevilacqua, Domenico Barone, Silvia Malavasi, and Giampaolo Gavelli. Automatic detection of misleading blood flow values in CT perfusion studies of lung cancer. *Biomedical signal processing and control*, 26:109–116, 2016.

[29] Alessandro Bevilacqua, Giampaolo Gavelli, Serena Baiocco, and Domenico Barone. CT Perfusion in Patients with Lung Cancer: Squamous Cell Carcinoma and Adenocarcinoma Show a Different Blood Flow. *BioMed Research International*, 2018, 2018.

[30] Meghan G. Lubner, Andrew D Smith, Kumar Sandrasegaran, Dushyant V. Sahani, and Perry J. Pickhardt. CT Texture Analysis: Definitions, Applications, Biologic Correlates, and Challenges. *Radiographics*, 37(5):1483–1503, 2017.

[31] Balaji Ganeshan, Kenneth A Miles, Rupert CD Young, and Chris R Chatwin. Hepatic enhancement in colorectal cancer: texture analysis correlates with hepatic hemodynamics and patient survival. *Academic radiology*, 14(12):1520–1530, 2007.

[32] K Skogen, B Ganeshan, T Good, G Critchley, and KA Miles. Imaging heterogeneity in gliomas using texture analysis. *Cancer Imaging*, 11:S113, 2011.

[33] Jae-Hun Kim, Eun Sook Ko, Yaeji Lim, Kyung Soo Lee, Boo-Kyung Han, Eun Young Ko, Soo Yeon Hahn, and Seok Jin Nam. Breast cancer heterogeneity: MR imaging texture analysis and survival outcomes. *Radiology*, 282(3):665–675, 2016.

[34] M Craigie, J Squires, and K Miles. Can CT measures of tumour heterogeneity stratify risk for nodal metastasis in patients with non-small cell lung cancer? *Clinical radiology*, 72(10):899–e1, 2017.

[35] Franca Wagner, Yahya Ali Hakami, Geoffrey Warnock, Gabriel Fischer, Martin W Huellner, and Patrick Veit-Haibach. Comparison of contrast-enhanced CT and [18F] FDG PET/CT analysis using kurtosis and skewness in patients with primary colorectal cancer. *Molecular imaging and biology*, 19(5):795–803, 2017.